Mon. Not. R. Astron. Soc. **000**, 000–000 (0000) Printed 3 February 2015 (MN LATEX style file v2.2)

The Mass-Concentration Relation and the Stellar-to-Halo Mass Ratio in the CFHT Stripe 82 Survey

HuanYuan Shan[1⋆], Jean-Paul Kneib[1,2], Ran Li[3], Johan Comparat[4,5], Thomas Erben[6], Martin Makler,[7] Bruno Moraes,[8,9] Ludovic Van Waerbeke,[10], James E. Taylor[11], Aldée Charbonnier[12]

[1]*Laboratoire d'astrophysique (LASTRO), Ecole Polytechnique Fédérale de Lausanne (EPFL), Observatoire de Sauverny, CH-1290 Versoix, Switzerland*
[2]*Aix Marseille Université, CNRS, LAM (Laboratoire d'Astrophysique de Marseille) UMR 7326, 13388, Marseille, France*
[3]*Key Laboratory for Computational Astrophysics, The Partner Group of Max Planck Institute for Astrophysics, National Astronomy Observatory, Chinese Academy of Sciences, Beijing 100871, China*
[4]*Departamento de Fisica Teorica, Universidad Autonoma de Madrid, Spain*
[5]*Instituto de Fisica Teorica UAM/CSIC, Spain*
[6]*Argelander Institute for Astronomy, University of Bonn, Auf dem Hügel 71, 53121 Bonn, Germany*
[7]*Centro Brasileiro de Pesquisas Físicas, Rua Dr Xavier Sigaud 150, CEP 22290-180, Rio de Janeiro, RJ, Brazil*
[8]*Department of Physics and Astronomy, University College London, Gower Street, London, WC1E 6BT, UK*
[9]*CAPES Foundation, Ministry of Education of Brazil, Brasilia/DF 70040-020, Brazil*
[10]*Department of Physics and Astronomy, University of British Columbia, 6224 Agricultural Road, Vancouver, V6T 1Z1, BC, Canada*
[11]*Department of Physics and Astronomy, University of Waterloo, 200 University Avenue West, Waterloo, Ontario, Canada N2L 3G1*
[12]*Observatório do Valongo, Universidade Federal do Rio de Janeiro, Ladeira do Pedro Antônio 43, Saúde, Rio de Janeiro, RJ 20080-090, Brazil & Centro Brasileiro de Pesquisas Físicas, Rua Dr. Xavier Sigaud 150, Rio de Janeiro, RJ 22290-180, Brazil*

Accepted .... Received ...; in original form ...

ABSTRACT

We present a new measurement of the mass-concentration relation and the stellar-to-halo mass ratio over a $5 \times 10^{12} M_{\odot}$ to $2 \times 10^{14} M_{\odot}$ mass range. To achieve this, we use the CFHT Stripe 82 Survey (CS82) weak lensing data combined with a well defined catalog of clusters (the redMaPPer catalogue) and the LOWZ/CMASS galaxies of the Sloan Digital Sky Survey-III Baryon Oscillation Spectroscopic Survey Tenth Data Release (SDSS-III BOSS DR10). The stacked lensing signals around these samples are modeled as a sum of contributions from the central galaxy, the dark matter halo, and the neighboring halos. We measure the mass-concentration relation: $c_{200}(M) = A(\frac{M_{200}}{M_0})^B$ with $A = 5.25 \pm 1.67, B = -0.13 \pm 0.12$ for $0.2 < z < 0.4$ and $A = 6.77 \pm 1.13, B = -0.15 \pm 0.06$ for $0.4 < z < 0.6$. We conclude that the amplitude A and slope B are both consistent with the simulation predictions by Klypin et al. (2014) within the errors. We also measure the stellar-to-halo mass ratio and find it to be flatter than previous measurement for high stellar masses because of the complex structures and merger history in massive dark matter halos.

Key words: large-scale structure of Universe-gravitational lensing: weak-galaxies: clusters cosmology: theory dark matter

1 INTRODUCTION

Dark Matter (DM) is the dominant mass component in the universe. The hierarchical cold DM model with a cosmological constant (ΛCDM) is successful in explaining many observations on large-scale structures. The Navarro-Frenk-White (NFW) density profile (Navarro et al. 1997), which has been derived from DM only simulations, provides an accurate description of the dark matter density profile over most radii, can be described by just two parameters: the concentration and the mass enclosed in a region with a mean density above some given threshold.

Simulations have shown that these two parameters are correlated, with the average concentration of a halo being a weakly decreasing function of mass (e.g. NFW; Bullock et al. 2001; Hennawi et al. 2007; Duffy et al. 2008; Prada et al. 2012). With the latest MultiDark simulations, Klypin et al. (2014) provide a more accurate analytical fit for dark matter halo density profiles and concentrations.

However, the mass-concentration (*m-c* hereafter) relation is different in the exact form as measured in simulations and esti-

⋆ E-mail: huanyuan.shan@epfl.ch

mated from observations (e.g. Bullock et al. 2001; Comerford & Natarajan 2007; Hennawi et al. 2007; Duffy et al. 2008; Maccio et al. 2008; Mandelbaum et al. 2008; Oguri et al. 2009, 2012; Okabe et al. 2010; Sereno & Covone 2013; Foëx et al. 2014). For example, considering a sample of 28 galaxy clusters whose radial profiles are well constrained from combining weak and strong lensing data, Oguri et al. (2012) found a steeper function of mass, with the slope $\sim -0.59 \pm 0.12$. Merten et al. (2014) and Umetsu et al. (2014) studied the *m-c* relation with the Cluster Lensing and Supernova Survey with Hubble (CLASH) data, which is in excellent agreement with simulations when the CLASH X-ray selection function and projection effects are taken into account. Du & Fan (2014) studied the bias from the miscentering problem, selection effects and shape noise from intrinsic ellipticity of background galaxies on the measurement of *m-c* relation with individual clusters. They found that the existence of noise can compensate the miscentering problem and reduce the systematic bias although the scatters of mass and concentration get considerably larger.

Mandelbaum et al. (2008) performed a statistical analysis to estimate the *m-c* relation over three orders of magnitude in mass using the stacked weak lensing signals of galaxies, groups and clusters in Sloan Digital Sky Survey (SDSS). Their analysis used the information outside the halo central region in order to avoid regions where baryons dominate, and to minimize errors from misestimation of clusters' centers. They found an *m-c* relation with a slope consistent with simulations, but an amplitude that is about 2σ below theoretical expectations. With the SDSS-III/Constant Mass (CMASS) galaxies in the Canada-France-Hawaii Telescope Lensing Survey (CFHTLenS), Miyatake et al. (2013) also showed a 20% smaller concentration than the theoretical predictions. With the CFHTLenS catalog and photometrically selected clusters, Covone et al. (2014) found an over-concentrated but flat relation.

Galaxy properties, such as luminosity or stellar mass, are tightly coupled to the DM halo mass. The link between the stellar and DM halos is critical for understanding the formation and evolution of galaxies. The observed luminosity of the central galaxy is always used to fix the stellar mass component. There are several methods to measure the stellar-to-halo mass relation (*SHMR*) including stellar kinematics (Conroy et al. 2007; More et al. 2011), abundance matching (Moster et al. 2010; Behroozi et al. 2010), the Tully-Fisher relation (Pizagno et al. 2007; Miller et al. 2014) and weak lensing (Mandelbaum et al. 2006; Leauthaud et al. 2012; Velander et al. 2014; Hudson et al. 2015; Han et al. 2015). In particular, Leauthaud et al. (2012) found that the slope of the *SHMR* rises sharply at $M_* >\sim 4.5 \times 10^{10} M_\odot$.

In this paper, we use a sample of redMaPPer clusters (Rykoff et al. 2014), the LOWZ and CMASS galaxies of SDSS-III BOSS DR10 and the shear catalog from the CFHT Stripe 82 dataset to measure the tangential shear, and quantify the *m-c* relation and the *SHMR*.

2 OBSERVATIONAL DATA

2.1 The Source catalog

The source galaxies used in our measurement are taken from the CFHT Stripe 82 Survey (CS82: Erben et al. 2015), which is an *i*-band imaging survey covering a large fraction of SDSS Stripe 82 region with a median seeing 0.59". The survey contains a total of 173 tiles with 165 from CS82 and 8 f rom CFHT-LS Wide. Each CS82 tile was obtained from 4 consecutive dithered observations each with an exposure time of 410 seconds. The completeness magnitude is $i_{AB} \sim 24.0$.

The shapes of faint galaxies are measured with the *lensfit* method (Miller et al 2007, 2013). In this work we use the same pipeline as the CFHTLenS collaboration. Therefore the shear calibration factors described in Heymans et al. (2012) can be directly applied to our data.

We use all galaxies with weight $w > 0$, FITCLASS=0 and MASK$\leqslant$1, in which w represents an inverse variance weight assigned to each source galaxy by *lensfit*, FITSCLASS is a star/galaxy classification provided by *lensfit*. The parameter MASK describes the mask information at an object's position. Objects with MASK$\leqslant$1 can safely be used for most weak lensing analyses (Erben et al. 2013). After masking out bright stars and other image artifacts, the effective sky coverage is $\sim$130deg^2.

As CS82 contains only *i*-band, we derive the photometric redshifts (photo-z) using *EAZY* (Brammer et al. 2008) for the source galaxies from the overlapping multi-color co-add data from SDSS (Annis et al. 2014). The total number of source galaxies that pass the aforementioned cuts and have an available photo-z is $4,449,618$ ($\sim 9.5 gals/arcmin^2$).

2.2 Lens selection

We use the redMaPPer clusters and LOWZ/CMASS galaxies in two redshift bins, $0.2 < z < 0.4$ and $0.4 < z < 0.6$, as lenses:

(1) The RedMaPPer Cluster Catalog:

The redMaPPer cluster catalog by Rykoff et al. (2014) is based on the optimized red-sequence richness estimator λ. The richness λ is the number of red sequence galaxies brighter than $0.2L_*$ at the redshift of the cluster within a scaled aperture. The redMaPPer cluster catalog in CS82, which is obtained from the SDSS Stripe 82 coadd using the CS82 object detections, covers the redshift range $0.1 < z < 0.6$. The objects with richness $\lambda > 15$ correspond to the halo mass $\sim 8 \times 10^{13}\ M_\odot$ (Erben et al. 2015). In order to reduce the effects of miscentering problem, we choose the clusters with well-defined centers $P_{cen} > 0.9$, which is the center probability. We then divide the clusters into two redshift bins with redshift $0.2 < z < 0.4$ and $0.4 < z < 0.6$. For both low and high redshift clusters, we divide them into two richness bins ($20 < \lambda < 30, 30 < \lambda < 200$) with $(57, 31)$ and $(96, 75)$ systems, respectively.

(2) LOWZ & CMASS Galaxy Catalog:

We also use the LOWZ and CMASS galaxy catalog from SDSS-III BOSS DR10 as lens galaxies[1]. The two samples are both the main SDSS-III BOSS BAO tracers (Dawson et al. 2013). LOWZ samples consist of red galaxies at $z < 0.4$ from the SDSS DR8 (Aihara et al. 2011) imaging data; CMASS samples are selected with an approximately constant stellar mass threshold (Eisenstein et al. 2011). Stellar masses of the two samples are from the Portsmouth SED-fitting (Maraston et al. 2013) based on the BOSS spectroscopic redshift. We choose the LOWZ and CMASS galaxies within redshift $0.2 < z < 0.4$ and $0.4 < z < 0.6$. We also divide them into 3 and 4 stellar mass bins, which will be used on the *SHMR* measurement, with $(2350, 2492, 2325)$ and $(5966, 6168, 7481, 7611)$ systems for the low-z and high-z range, respectively (see Figure 1).

[1] `https://www.sdss3.org/dr10/spectro/galaxy.php`

3 LENSING SIGNAL

We measure the *m-c* relation with stacked lensing signal. Stacking many halos reduces the fluctuations due to noise caused by uncorrelated structures along the line-of-sight, shape measurement noise, substructures, and the shape variations of individual halos. Thus, the measurement can determine the average mass profile. Furthermore, it allows for the lensing measurement of lower mass halos, where individual detection is impossible due to their smaller shears relative to clusters. Individual massive cluster observations and those based on stacked analysis of many halos are thus complementary, drastically increasing the available baseline in mass.

Except the dark matter halos, the models for the lensing signals include the following components:

(1) Gavazzi et al. (2007) found that a central baryonic component is required to fit both the strong and weak lensing profiles of early-type galaxies in the SLACS survey. This component can be simply modeled as a point mass (e.g., Leauthaud et al. 2012).

(2) In order to measure the lensing signals, locating the centers of dark matter halos is very important because miscentering can add significant systematic uncertainties. In general, halo centers are typically assumed to be traced by a central galaxy. However, it has been argued that these assumptions may not be entirely true and that central galaxies could be "sloshing" around in the dark matter halo potential well (e.g. van den Bosch et al. 2005; Gao & White 2006; Johnston et al. 2007; Hikage et al. 2013). As in Johnston et al. (2007), Leauthaud et al. (2010), George et al. (2012) and Li et al. (2014), centroid errors will lead to a smoothing of the lensing signal on small scales and to an underestimate of halo masses. The distribution of miscentering can be described by a 2D Gaussian distribution:

$$P(R_{\rm off}) = \frac{R_{\rm off}}{\sigma_{\rm off}} \exp\left(-\frac{1}{2}(R_{\rm off}/\sigma_{\rm off})^2\right), \quad (1)$$

where $R_{\rm off}$ is the distance between the halo center and central galaxy position, $\sigma_{\rm off}$ is the effective scale length. This model is from mock catalogs by Johnston et al. (2007), which is consistent with the measurement from 2D lensing shear maps of 25 massive clusters by Oguri et al. (2010).

(3) At the large scales, the neighboring halos contribute to the lensing profile (Johnston et al. 2007; Cacciato et al. 2009, Li et al. 2009, Oguri & Hamana 2011). The tangential shear profile due to the neighboring halos is

$$\gamma_{2h}(\theta; M, z) = \int \frac{ldl}{2\pi} J_2(l\theta) \frac{\bar{\rho}_m(z) b_h(M)}{(1+z)^3 \Sigma_{\rm crit} D_A^2(z)} P_m(k_l; z), \quad (2)$$

where J_2 is the second order Bessel function, $\bar{\rho}_m(z)$ is the mass density at z, $D_A(z)$ is the angular diameter distance, $P_m(k)$ is the linear matter power spectrum, $\Sigma_{\rm crit}$ is the critical mass density, and $b_h(M)$ is the halo bias that we take from Tinker et al. (2010).

Combining all the contributions, the lensing signal $\Delta\Sigma$ can be written as:

$$\Delta\Sigma(R) = \frac{M_p}{\pi R^2} + p_{\rm cen}\Delta\Sigma_{\rm NFW}(R) + (1 - p_{\rm cen})\Delta\Sigma^{\rm off}_{\rm NFW}(R|P_{\rm off}) + \Delta\Sigma_{2h}(R), \quad (3)$$

where sequentially, the terms come from the contribution of central baryonic components, the dark matter halos, the miscentering halos, and the neighboring halos. The model is described by 5 parameters: the halo mass $M_{\rm vir}$, the concentration $c_{\rm vir}$, the central baryonic mass M_p, the effective scale length $\sigma_{\rm off}$ and the probability $p_{\rm cen}$ that the centers we use here are accurately centered on the dark matter halos.

To obtain $\Delta\Sigma$ we stack lens-source pairs in 8 logarithmic radial (R) bins from 0.1 to 10 Mpc h^{-1}. For a sample of selected lenses, $\Delta\Sigma(R)$ is estimated using

$$\Delta\Sigma(R) = \frac{\sum_{ls} w_{ls} \gamma_t^{ls} \Sigma_{\rm crit}}{\sum_{ls} w_{ls}}, \quad (4)$$

where γ_t^{ls} is the tangential shear, $w_{ls} = w_n \Sigma_{\rm crit}^{-2}$, and w_n is a weight factor introduced to account for intrinsic scatter in ellipticity and shape measurement error.

With the multiplicative errors m taken into account statistically (Miller et al. 2013), we apply it to the average shear measurement in both the low-z and high-z samples using the correction as Velander et al. (2014) and Hudson et al. (2015):

$$1 + K(z_l) = \frac{\sum_{ls} w_{ls}(1+m)}{\sum_{ls} w_{ls}}. \quad (5)$$

The lensing signal can be calibrated as follows:

$$\Delta\Sigma^{\rm cal}(R) = \frac{\Delta\Sigma(R)}{1 + K(z_l)}. \quad (6)$$

The effect of this correction term is to increase the average lensing signals by $\sim 5.5\%$ and 6.2% at $0.2 < z < 0.4$ and $0.4 < z < 0.6$, respectively.

To minimize the contamination due to photo-z uncertainties of the source galaxies, we remove the lens-source pairs with $z_s - z_l < 0.1$.

4 RESULTS

We show the observed galaxy-galaxy lensing signals for the low and high redshift samples in Figure 1. The black circles with error bars represent the measured excess surface mass density. We fit them to the model described in section 3. The black solid curves shows the best-fit results with all the components. The different model components are shown in dashed curves: the central baryonic matter (red), the dark matter halo profile (green), the miscentering halo component (blue) and neighboring halos (magenta). At small scales (0.1 − 1Mpc), the dark matter halo is the dominant component. At large scales (> 3Mpc for galaxies and > 5Mpc for clusters), the neighboring halos contribute more. The best-fit results are given in Table 1. We convert the measured $M_{\rm vir}$ and $c_{\rm vir}$ to M_{200} and c_{200} with the formula by Johnston et al. (2007). The stellar masses M_* of LOWZ/CMASS galaxies are from the Portsmouth SED-fitting (Maraston et al. 2013) based on the SDSS-III BOSS DR10 data. M_* of the redMaPPer clusters are estimated by matching the positions of central galaxies with the galaxy catalog of SDSS DR10. The fitted probability $p_{\rm cen}$ are all close to 1, which indicates that: (1) the centers of redMaPPer clusters are well defined; (2) LOWZ/CMASS galaxies are almost all central galaxies, $\sim 10\%$ of them may be the most luminous satellite galaxies as the clustering analysis by Parejko et al. (2013) and White et al. (2011).

4.1 *m-c* relation

The *m-c* relation from the simulation predictions is given as:

$$c_{200}(z, M) = A\left(\frac{M_{200}}{M_0}\right)^B (1+z)^C, \quad (7)$$

with $M_0 = 2.0 \times 10^{12} M_\odot h^{-1}$. As we cannot get a redshift dependence relation with only two redshift bins, the redshift dependence

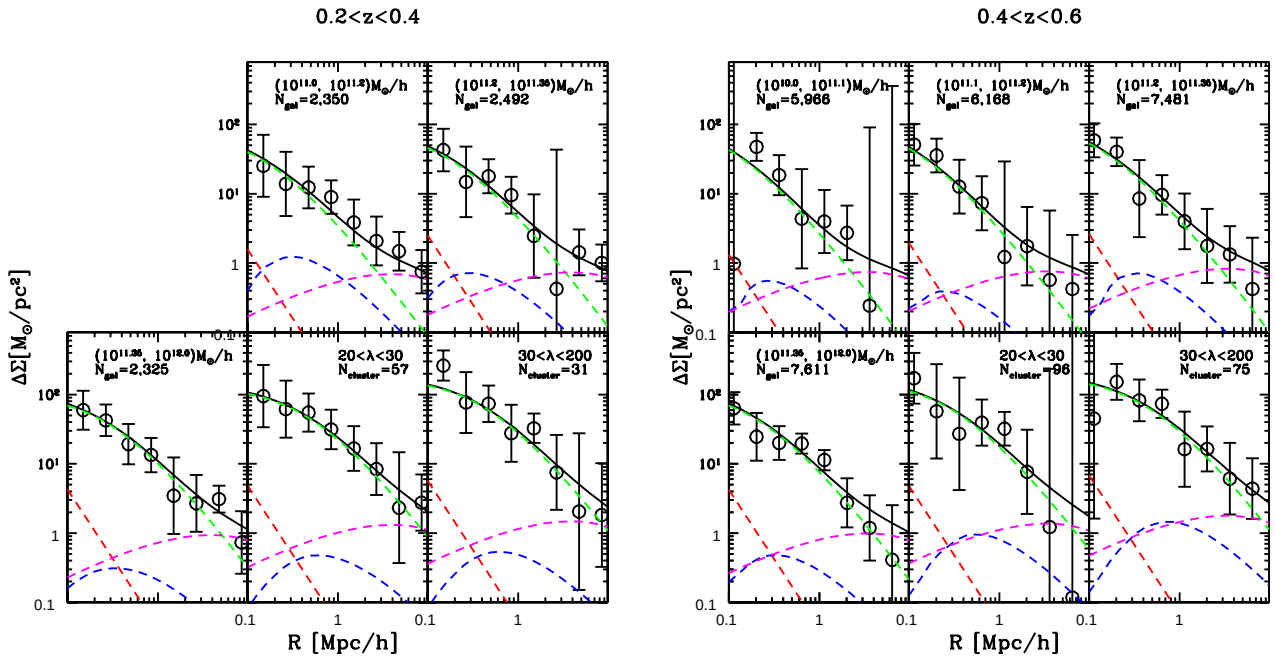

Figure 1. Best-fit model for the low (left) and high (right) redshift samples (black solid lines). Black circles show the measured excess surface mass density $\Delta\Sigma$ of both LOWZ/CMASS galaxies and clusters with different bins (clusters: Bottom-middle and bottom-right panels; LOWZ/CMASS: others). The model components are the central baryonic matter (red), the dark matter halo profile (green), the miscentering halo component (blue) and neighboring halos (magenta).

Table 1. Density Profile Models in Figure 1.

	z	$M_{\rm vir}$ $10^{14}M_\odot/h$	$c_{\rm vir}$	M_{200} $10^{14}M_\odot/h$	c_{200}	M_* $10^{12}M_\odot$	$\sigma_{\rm off}$ Mpc	$p_{\rm cen}$
$(10^{11.0}, 10^{11.2})M_\odot$	$0.2 < z < 0.4$	0.12 ± 0.04	4.66 ± 1.29	0.10 ± 0.03	3.80 ± 1.09	0.13 ± 0.10	0.45 ± 0.26	0.76 ± 0.18
$(10^{11.2}, 10^{11.35})M_\odot$	$0.2 < z < 0.4$	0.15 ± 0.04	4.19 ± 0.85	0.13 ± 0.03	3.41 ± 0.71	0.19 ± 0.17	0.30 ± 0.17	0.82 ± 0.13
$(10^{11.35}, 10^{12.0})M_\odot$	$0.2 < z < 0.4$	0.37 ± 0.07	3.60 ± 0.66	0.31 ± 0.06	2.91 ± 0.55	0.30 ± 0.27	0.19 ± 0.15	0.89 ± 0.10
$20 < \lambda < 30$	$0.2 < z < 0.4$	1.01 ± 0.09	3.15 ± 1.02	0.83 ± 0.073	2.54 ± 0.85	0.32 ± 0.25	0.55 ± 0.28	0.95 ± 0.12
$30 < \lambda < 200$	$0.2 < z < 0.4$	1.37 ± 0.36	3.66 ± 1.20	1.14 ± 0.30	2.96 ± 1.01	0.37 ± 0.21	0.63 ± 0.25	0.96 ± 0.11
$(10^{10.0}, 10^{11.1})M_\odot$	$0.4 < z < 0.6$	0.074 ± 0.03	5.40 ± 1.51	0.067 ± 0.03	4.62 ± 1.31	0.095 ± 0.056	0.32 ± 0.17	0.86 ± 0.15
$(10^{11.1}, 10^{11.2})M_\odot$	$0.4 < z < 0.6$	0.083 ± 0.03	5.00 ± 0.97	0.074 ± 0.03	4.26 ± 0.84	0.14 ± 0.11	0.23 ± 0.12	0.87 ± 0.13
$(10^{11.2}, 10^{11.35})M_\odot$	$0.4 < z < 0.6$	0.12 ± 0.05	4.69 ± 0.91	0.11 ± 0.04	3.99 ± 0.79	0.19 ± 0.15	0.40 ± 0.17	0.86 ± 0.12
$(10^{11.35}, 10^{12.0})M_\odot$	$0.4 < z < 0.6$	0.24 ± 0.06	3.88 ± 0.82	0.22 ± 0.04	3.28 ± 0.70	0.30 ± 0.18	0.24 ± 0.14	0.88 ± 0.21
$20 < \lambda < 30$	$0.4 < z < 0.6$	0.68 ± 0.11	3.62 ± 1.11	0.60 ± 0.084	3.06 ± 0.96	0.33 ± 0.21	0.57 ± 0.33	0.91 ± 0.21
$30 < \lambda < 200$	$0.4 < z < 0.6$	1.39 ± 0.30	3.35 ± 0.52	1.20 ± 0.26	2.83 ± 0.45	0.47 ± 0.28	0.68 ± 0.21	0.90 ± 0.33

Notes: M_* is the stellar mass from the Portsmouth SED-fitting (Maraston et al. 2013) based on the SDSS-III BOSS DR10 data.

is calculated with the mass and concentration with Multidark simulations of Klypin et al. (2014). Because of the upturn of the concentrations at large masses regime of high redshift, the redshift dependence C ~ -0.67 is fitted with the DM halos of Multidark in the redshift region $0.0 < z < 0.6$, which is suitable to the data in our analysis. The best-fit *m-c* relations are shown in Table 2. Because of the bigger errors on low-z sample, the *m-c* relations of both samples are consistent.

Giocoli et al. (2012) found that the halo triaxiality and the substructures within the host halo virial radius can bias the *m-c* relation. They propose a method for correcting the *m-c* relation for the projection effects and also for adiabatic contraction:

$$c_{2D}(M) = c_{3D}(M) \times 1.630 M^{-0.018}, \quad (8)$$

In Figure 2, we show the results on the 3D corrected *m-c* relation after rescaling the results to $z = 0$. The 3D correction is used on all the observational dataset and simulation predictions.

Table 2. Best-fit Mass-Concentration relations.

z	A	B
$0.2 < z < 0.4$	5.25 ± 1.67	-0.13 ± 0.12
$0.4 < z < 0.6$	6.77 ± 1.13	-0.15 ± 0.06

With the 3D corrections by Giocoli et al. (2012), we can directly compare our measurements with the three-dimensional (3D) N-body simulation results. Comparing with the results by Duffy et al. (2008) and Klypin et al. (2014), the amplitudes A and slopes B of both redshift samples are consistent with the simulation predictions within the errors.

We then compare our results with previous measurements. The 3D corrections by Giocoli et al. (2012) are used on these measurements.

By stacking weak lensing signals of galaxies, groups and clusters from SDSS dataset, Mandelbaum et al. (2008) fit the data to the

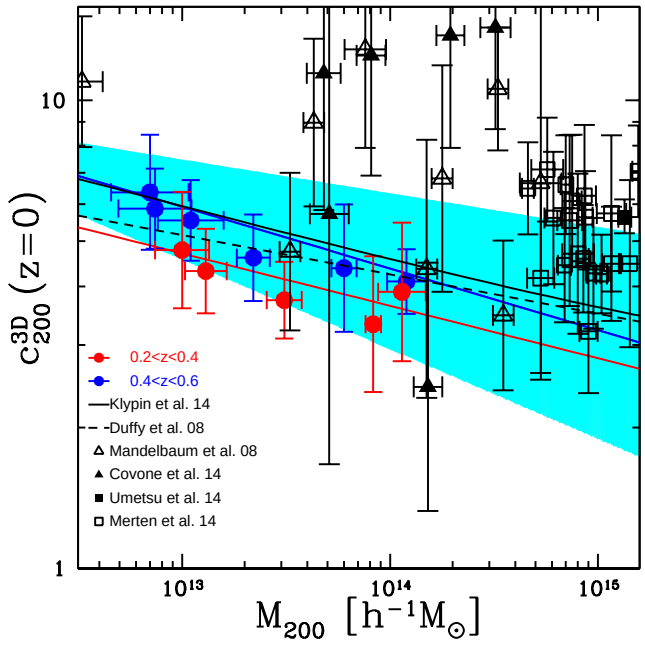

Figure 2. 3D corrected *m-c* relation with clusters and galaxies in CS82 after rescaling all the results to $z = 0$. Red and blue circles denote the stacked lensing signals from low and high redshift samples, respectively. The red curve is the best-fit *m-c* relation of the low redshift sample. The blue curve and cyan-shaded area is best-fit *m-c* relation of the high redshift sample and its 1σ uncertainty. Black curves are the simulation predictions by Duffy et al. (2008) (dashed) and Klypin et al. (2014) (solid). The black symbols denote the measurement on mass and concentration by Mandelbaum et al. (2008) with SDSS; Covone et al. (2014) with CFHTLenS; Umetsu et al. (2014) and Merten et al. (2014) with CLASH cluster sample.

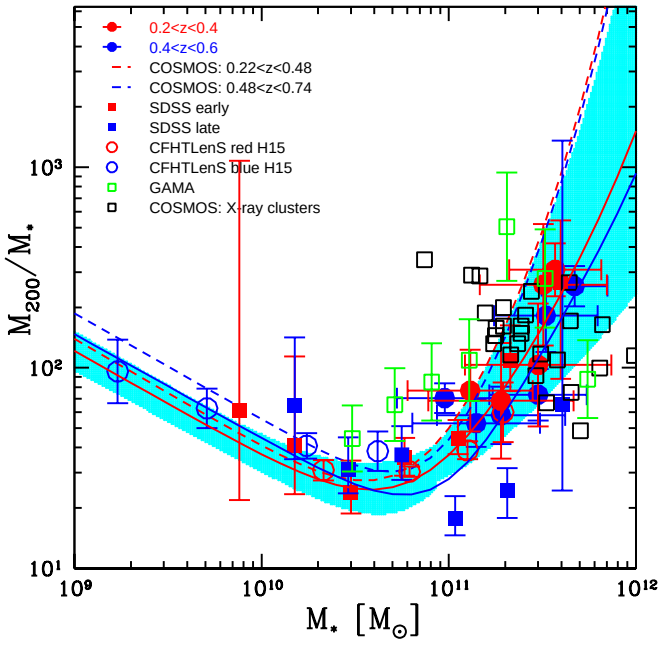

Figure 3. Halo-to-stellar mass ratio as a function of stellar mass. Red and blue dots denote the measurements from low and high redshift samples, respectively. The red solid curve and cyan-shaded area is the best-fit *SHMR* relation of our low redshift sample combined with H15 and its 1σ uncertainty. The blue solid curve is the best-fit *SHMR* relation of our high redshift sample combined with H15. The red and blue dashed curves are the fitted relation by the COSMOS measurements We compare our measurements with other galaxy-galaxy lensing measurements, including SDSS (Mandelbaum et al. 2006), CFHTLenS (H15), COSMOS (Leauthaud et al. 2012), COSMOS X-ray clusters (Leauthaud et al. 2010), and GAMA (Han et al. 2015).

model assuming a spherical NFW profile excluding small scales to reduce the effects of baryons and miscentering halos. As shown in Figure 2, their measurements are comparable to ours, but more scattered.

With photo-z selected clusters (Wen et al. 2009) in the CFHTLenS data, Covone et al. (2014) measured the mass and concentration by stacking shear profiles. The measured concentrations in four richness bins are higher than the simulation predictions and generate a flat and over-concentrated mass-concentration relation.

A possible reason might be the choice of the cluster catalog. Wen's cluster finder purely based on the photo-z of galaxies. The richness of some clusters may be overestimated due to the inaccuracy of photo-z. A detail comparison will need to be carried on in future.

The recent CLASH measurements for individual clusters (Merten et al. 2014) and stacking (Umetsu et al. 2014) focus on more massive strong lensing clusters $\sim 10^{15} M_\odot h^{-1}$, which give large concentrations. Accounting for the CLASH selection function based on X-ray morphology and projections effects inherent in lensing observations (Meneghetti et al. 2014), a better agreement can be found between observations and theoretical predictions.

4.2 *SHMR* measurement

With the measurement of stellar mass, we can also estimate the *SHMR*. Following Leauthaud et al. (2012), $f_{SHMR}(M_h)$ is mathematically defined via its inverse function:

$$\log_{10}(f^{-1}_{SHMR}(M_h)) = \log_{10}(M_1) + \beta \log_{10}\left(\frac{M_*}{M_{*,0}}\right) + \frac{\left(\frac{M_*}{M_{*,0}}\right)^{\delta}}{1+\left(\frac{M_*}{M_{*,0}}\right)^{-\gamma}} - \frac{1}{2}, \quad (9)$$

where M_1 is a characteristic DM halo mass, $M_{*,0}$ is a characteristic stellar mass, β is the low-mass *SHMR* slope, δ and γ is the high-mass *SHMR* slope. In Figure 3, we show the results of this paper in addition to other galaxy-galaxy lensing studies, including the measurement in SDSS (Mandelbaum et al. 2006), CFHTLenS (Hudson et al. 2015 (H15)), the Cosmic Evolution Survey (COSMOS: Leauthaud et al. 2010, 2012) and the Galaxy And Mass Assembly (GAMA: Han et al. 2015). Our measurement of M_{200}/M_* is ideally combined with the results of H15, as they provide very good estimates of the *SHMR* at the same redshift bins as ours and covering smaller masses. Our best fit results for this combined dataset are given in Table 3.

We compare our results with the best-fit in Leauthaud et al. (2012). At low stellar mass ($M_* < 4 \times 10^{10} M_\odot$), the constraints are only from H15. The behaviors of *SHMR* are similar. The major halo mergers are minor galaxy mergers in this regime. The growth of stellar mass through the effects of mergering will be limited compared to the growth of DM halo mass. At $M_* \sim 4 - 6 \times 10^{10} M_\odot$, M_{200}/M_* of the results reaches a minimum, which reflects the most

Table 3. Best-fit results of *SHMR*.

z	$\log_{10}(M_1)$	$\log_{10}(M_{*,0})$	β	δ	γ
$0.2 < z < 0.4$	12.51 ± 0.047	10.97 ± 0.032	0.47 ± 0.019	0.43 ± 0.11	1.45 ± 0.27
$0.4 < z < 0.6$	12.69 ± 0.056	11.13 ± 0.035	0.48 ± 0.022	0.44 ± 0.15	1.90 ± 0.31

efficient star formation rate at such a mass. The minimum values are consistent with the COSMOS measurements within the errors. At low stellar mass regime, the DM halos are dominated by single central galaxies, the supernovae feedback could be the main reason to prevent the star formation. At high stellar mass, we find a relatively flatter slope. The scatter should be due to the appearance of hot gas in the massive DM halos, making more complex merger history.

5 CONCLUSIONS

Combing two different redshift samples of redMaPPer clusters and LOWZ/CMASS galaxies with the shear catalog of CS82, we fit the lensing signals around these clusters and massive galaxies including the effects of baryons, miscentering halos, and neighboring halos, and study the *m-c* relation and also the *SHMR*.

Our main results are as follows:

1. We find that the concentration decreases weakly with mass, $c = A(M/M_0)^B$ with the amplitude A and slope B in good agreement with the previous measurement by Mandelbaum et al. (2008). Including the 3D correction suggested by Giocoli et al. (2012), the two parameters are also consistent with simulation predictions within the errors.

Klypin et al. (2014) also shows that the NFW profile can systematically overpredict the halo concentration by $10-20\%$ for the massive halo density profile. The Einasto profile can provide a more accurate measurement. However, the current precision of data cannot distinguish between the two profiles. The lensing signals in the inner region of dark matter halos have large error bars. Mandelbaum et al. (2008) found a very similar *m-c* relation for the NFW and Einasto profiles with SDSS data. Using the recent CLASH, Umetsu et al. (2014) found similar mass and concentration of the two profiles. In order to compare the two profiles, we also fit the lensing signals of the redMaPPer clusters with the Einasto profile, and find similar *m-c* relation as with the NFW profile. We conclude that the current data can not distinguish the two profiles.

2. Combining previous galaxy-galaxy lensing measurements, we measure a relatively flatter slope of the *SHMR* at high stellar mass. With COSMOS data, Leauthaud et al. (2012) found a steeper slope of the *SHMR* at $M_* > 4.5 \times 10^{10} M_\odot$.

The flatter slope of the *SHMR* at high stellar mass implies the massive DM halos contain more complex structures and merger history. The scatter at the high stellar mass regime could be due to the appearance of hot gas in the massive DM halos, making a more complex merger history.

In our analysis, we use the stellar mass of central galaxy for the redMaPPer clusters. There could be more than one central galaxy in a cluster, however, making our measurement a lower limit on the total stellar mass in a halo. Such an effect could raise the *SHMR* at high stellar mass regime and increase the scatter.

With future wide surveys (DES/HSC/LSST/EUCLID), we expect to measure more accurate the *m-c* relation and the *SHMR*, and test for possible measured bias.

ACKNOWLEDGMENTS

This work is based on observations obtained with MegaPrime/MegaCam, a joint project of CFHT and CEA/DAPNIA, at the Canada-France-Hawaii Telescope (CFHT), which is operated by the National Research Council (NRC) of Canada, the Institut National des Science de l'Univers of the Centre National de la Recherche Scientifique (CNRS) of France, and the University of Hawaii. The Brazilian partnership on CFHT is managed by the Laboratório Nacional de Astrofísica (LNA). This work made use of the CHE cluster, managed and funded by ICRA/CBPF/MCTI, with financial support from FINEP and FAPERJ. We thank the support of the Laboratório Interinstitucional de e-Astronomia (LIneA). We thank the CFHTLenS team for their pipeline development and verification upon which much of this surveys pipeline was built.

The authors thank Francisco Prada and Charling Tao for useful discussions. This research was supported by a Marie Curie International Incoming Fellowship within the 7^{th} European Community Framework Programme. HYS acknowledges the support from Swiss National Science Foundation (SNSF) and NSFC of China under grants 11103011. JPK acknowledges support from the ERC advanced grand LIDA. LR acknowledges the NSFC grants (No.11303033) and the support from Youth Innovation Promotion Association of CAS. JC acknowledges financial support from MINECO (Spain) under project number AYA2012-31101. TE is supported by the Deutsche Forschungsgemeinschaft through the Transregional Collaborative Research Centre TR 33 - 'The Dark Universe'. BM acknowledges financial support from the CAPES Foundation grant 12174-13-0. MM is partially supported by CNPq (grant 486586/2013-8) and FAPERJ (grant E-26/110.516/2-2012).

REFERENCES

Aihara, H., et al., 2011, ApJS, 193, 29
Annis, J., et al., 2014, ApJ, 794, 120
Brammer, G.B., van Dokkum, P.G., & Coppi, P., 2008, ApJ, 686, 1503
Behroozi, P. S., Conroy, C., & Wechsler, R. H., 2010, ApJ, 717, 379
Comerford J. M., Natarajan P., 2007, MNRAS, 379, 190
Conroy, C., Prada, F., Newman, J. A., et al., 2007, ApJ, 654, 153
Covone G., Sereno M., Kilbinger M., Cardone V. F., 2014, ApJ, 784, L25
Cacciato, M., van den Bosch, F. C., More, S., Li, R., Mo, H. J., Yang, X., 2009, MNRAS, 394, 929
Dawson, K. S., Schlegel, D. J., Ahn, C. P., et al., 2013, AJ, 145, 10
Duffy A. R., Schaye J., Kay S. T., & Dalla Vecchia C., 2008, MNRAS, 390, L64
Du, W. & Fan, Z.H., ApJ, 2014, 785, 57
Eisenstein, D.J., et al., 2011, AJ, 142, 72
Erben, T., Hildebrandt, H., Miller, L., van Waerbeke, L., Heymans, C., Hoekstra, H., Kitching, T.D., Mellier, Y., 2013, MNRAS, 433, 2545

Erben, T., Kneib, J.-P., Leauthaud, A., et al., 2015, in preparation
Foëx, G., Motta, V., Jullo, E., Limousin, M., & Verdugo, T., 2014, A&A, 572, 19
Gavazzi, R., Treu, T., Rhodes, J. D., Koopmans, L. V. E., Bolton, A. S., Burles, S., Massey, R. J., & Moustakas, L. A., 2007, ApJ, 667, 176
Gao, L., & White, S. D. M., 2006, MNRAS, 373, 65
George, M. R., Leauthaud, A., Bundy, K., et al., 2012, ApJ, 757, 2
Giocoli, C., Menghetti, M., Ettori, S., & Moscardini, L., 2012, MNRAS, 426, 1558
Han, J.X., Eke, V.R., Frenk, C.S., et al., 2015, MNRAS, 446, 1356
Hennawi J. F., Dalal N., Bode P., & Ostriker J. P., 2007, ApJ, 654, 714
Heymans, C., Van Waerbeke, L., Miller, L., et al., 2012, MNRAS, 427, 146
Hikage, C., Mandelbaum, R., Takada, M., & Spergel, D. N., 2013, MNRAS, 435, 2345
Hudson, M.J., Gillis, B.R., Coupon, J., et al., 2015, MNRAS, 447, 298
Johnston, D. E., Sheldon, E. S., Wechsler, R. H., et al., 2007, arXiv: 0709.1159
Klypin, A., Yepes, G., Gottlober, S., Prada, F., & Heb, S., 2014, arXiv: 1411.4001
Leauthaud, A., Finoguenov, A., Kneib, J.-P., et al., 2010, ApJ, 709, 97
Leauthaud, A., Tinker, J., Bundy, K., et al., 2012, ApJ, 744, 159
Leauthaud, A., George, M.R., Behroozi, P.S., et al., 2012, ApJ, 746, 95
Li, R., Mo, H. J., Fan, Z., Cacciato, M., van den Bosch, F. C., Yang, X., More, S., 2009, MNRAS, 394, 1016
Li, R., Shan, H.Y., Mo, H.J., et al., 2014, MNRAS, 438, 2864
Maccio A. V., Dutton A. A., van den Bosch F. C., 2008, MNRAS, 391, 1940
Mandelbaum, R., Seljak, U., Kauffmann, G., Hirata, C. M., & Brinkmann, J., 2006, MNRAS, 368, 715
Mandelbaum, R., Seljak, U., Hirata, C. M., 2008, JCAP, 8, 6
Maraston, C., et al., 2013, MNRAS, 435, 2764
Merten J. et al., 2014, arXiv:1404.1376
Meneghetti, M., et al., 2014, ApJ, 797, 34
Miyatake, H., More, S., Mandelbaum, R., Takada, M., Spergel, D. N., Kneib, J.-P., Schneider, D. P., Brinkmann, J., & Brownstein, J. R., 2013, arXiv:1311.1480
Miller, L., Kitching, T. D., Heymans, C., Heavens, A. F., & Van Waerbeke, L., 2007, MNRAS, 382, 315
Miller, L., Heymans, C., Kitching, T. D., et al., 2013, MNRAS, 429, 2858
Miller, S.H., Ellis, R.S., Newman, A.B., & Benson, A., 2014, ApJ, 782, 115
More, S., van den Bosch, F. C., Cacciato, M., et al., 2011, MNRAS, 410, 210
Moster, B. P., Somerville, R. S., Maulbetsch, C., et al., 2010, ApJ, 710, 903
Navarro J. F., Frenk C. S., White S. D. M., 1997, ApJ, 490, 493
Oguri, M. et al., 2009, ApJ, 699, 1038
Oguri, M., Takada, M, Okabe, N., Smith, G.P., 2010, MNRAS, 405, 2215
Oguri, M., & Hamana, T., 2011, MNRAS, 414, 1851
Oguri, M., Bayliss, M. B., Dahle, H., Sharon, K., Gladders, M. D., Natarajan, P., Hennawi, J. F., & Koester, B. P., 2012, MNRAS, 420, 3213
Okabe, N., Takada, M., Umetsu, K., Futamase, T., & Smith, G. P., 2010, PASJ, 62, 811
Parejko, J.K., Sunayama, T., Padmanabhan, N., et al., 2013, MNRAS, 429, 89
Pizagno, J., Prada, F., Weinberg, D. H., et al., 2007, AJ, 134, 945
Prada, F., Klypin, A. A., Cuesta, A. J., Betancort-Rijo, J. E., & Primack J., 2012, MNRAS, 423, 3018
Rykoff, E. S., Rozo, E., Busha, M. T., et al., 2014, ApJ, 785, 104
Sereno M., & Covone G., 2013, MNRAS, 434, 878
Tinker, J.L., Robertson, B.E., Kravtsov, A.V., Klypin, A., Warren, M. S., Yepes, G., Gottlober, S., 2010, ApJ, 724 878
Umetsu K. et al., 2014, ApJ, 795, 163
van den Bosch, Frank C., Tormen, G., & Giocoli, C., 2005, MNRAS, 359, 1029
Velander, M., van Uitert, E., Hoekstra, H., et al., 2014, MNRAS, 437, 2111
Wen, Z.L., Han, J.L., & Liu, F.S., 2009, ApJS, 183, 197
White, M., Blanton, M., Bolton, A., et al., 2011, ApJ, 728, 126